ORIGINAL PAPER

High-resolution lidar-based landslide hazard mapping and modeling, UCSF Parnassus Campus, San Francisco, USA

William C. Haneberg · William F. Cole · Gyimah Kasali

Abstract Airborne lidar (light detection and ranging) was used to create a high-resolution digital elevation model (DEM) and produce landslide hazard maps of the University of California, San Francisco Parnassus Campus. The lidar DEM consisted of nearly 2.8 million interpolated elevation values covering approximately 100 ha and posted on an 0.6 m horizontal grid, from which a set of 16 maps was produced. The first subset of maps showed aspects of the topography useful for landslide mapping, an engineering geological map and a qualitative slope hazard map. The second subset consisted of physics-based probabilistic landslide hazard maps for wet static, wet seismic, and dry seismic conditions. This case history illustrates the utility of lidar-based products, supplemented by field-based geological observations and physics-based probabilistic slope stability modeling, for the evaluation of existing and potential slope stability hazards on a steep and heavily forested site.

Keywords Lidar · Laser scanning · Landslides · Slope stability · Seismic slope stability · Digital terrain modeling · GIS

W. C. Haneberg (✉)
Haneberg Geoscience, 10208 39th Avenue SW,
Seattle, WA 98146, USA
e-mail: bill@haneberg.com

W. F. Cole
GeoInsite, 15919 Orange Blossom Lane,
Los Gatos, CA 95032, USA
e-mail: rockguy1@earthlink.net

G. Kasali
Rutherford & Chekene, 55 Second Street,
Ste. 600, San Francisco, CA 94105, USA
e-mail: GKasali@ruthchek.com

Résumé Le lidar (*light detection and ranging*) aéroporté a été utilisé pour créer un modèle numérique d'altitude (MNA) et pour produire des cartes de risque de glissement de terrain de l'Université de Californie, au Parnassus Campus à San Francisco. Le MNA lidar est composé de près de 2.8 millions de valeurs d'altitude calculées par interpolation couvrant environ 100 hectares et placées sur une grille cartographique horizontale de 0.6 m, duquelle une série de 16 cartes a été produite. Le premier sous-ensemble de cartes a révélé des aspects de la topographie utiles pour la cartographie des glissements de terrain, une carte de génie géologique et une carte qualitative des aléas en talus. Le second sous-ensemble consistait en des cartes probabilistes de risque de glissement de terrain basées sur la physique pour des conditions de pente statiques humides et sismiques sèches et humides. Cette étude de cas illustre l'utilité des produits à base de données lidar, complétés par des observations géologiques de terrain et par la modélisation probabiliste de la stabilité des pentes basée sur la physique, pour l'évaluation des aléas existants ou potentiels liés à la stabilité des pentes sur des sites fortement boisés et pentés.

Mots clés Lidar · Balayage laser · Glissements de terrain · Stabilité des pentes · La stabilité des pentes en conditions sismiques · Modélisation numérique des terrains · SIG

Introduction

Landslide hazard mapping in steep and heavily forested terrain is a difficult proposition for at least three reasons:

(1) Limited visibility and difficult access reduce the area that can be directly observed during field-based mapping;

(2) Aerial photograph interpretation can provide only limited information because landforms are obscured by vegetation;

(3) Conventional topographic maps derived from aerial photographs can be inaccurate or lack the detail necessary to identify actual or potential landslide hazards.

During the past decade, airborne lidar (an acronym for light detection and ranging)—also known as airborne laser scanning, airborne laser swath mapping, and laser altimetry—has provided practising geologists with a new way to create high-resolution digital elevation models (DEMs) and associated map products that allow accurate mapping of landforms even in areas covered by thick forest or jungle. The utility of airborne lidar-based maps and images for landslide hazard mapping and assessment has been shown in many parts of the United States, including the Puget Sound region of Washington (Schulz 2006; Troost et al. 2006), Oregon (Roering et al. 2005; Drazba et al. 2006), northern California (Falls et al. 2004; Stillwater Sciences 2007; Weppner et al. 2008a, b), Idaho (Glenn et al. 2005), North Carolina (Wooten et al. 2007), and Pennsylvania (Delano and Braun 2007), as well as other countries such as Papua New Guinea (Haneberg et al. 2005), Japan (Sato et al. 2007), Italy (Ardizzone et al. 2006), Belgium (Van Den Eeckhaut et al. 2006), and New Zealand (McKean and Roering 2004). The techniques used by these authors range from qualitative interpretation of shaded relief images to quantification of topographic roughness and implementation of physics-based mathematical models.

This paper describes the use of high-resolution airborne lidar data to support landslide hazard mapping and modeling of the steep and heavily forested Parnassus Campus of the University of California, San Francisco (Fig. 1). The process involved collecting project-specific airborne lidar data, processing the data to create a geologically optimal DEM and related derivative maps, performing qualitative engineering geological mapping, and conducting physics-based probabilistic landslide hazard modeling of extreme conditions for which the landslide hazard could not be evaluated on the basis of mapping alone. Although virtually all lidar data are good enough to produce DEMs of much higher resolution than conventional photogrammetric or satellite based DEMs, in this paper the term "high-resolution" is used in a special sense to describe lidar data with a higher than usual ground strike density as discussed below. The results were intended primarily to serve as a tool for campus-wide emergency planning and for obtaining a geological context for more detailed design-level geotechnical investigations undertaken for specific construction projects on campus. Although existing borehole logs were reviewed and incorporated into our interpretations, this
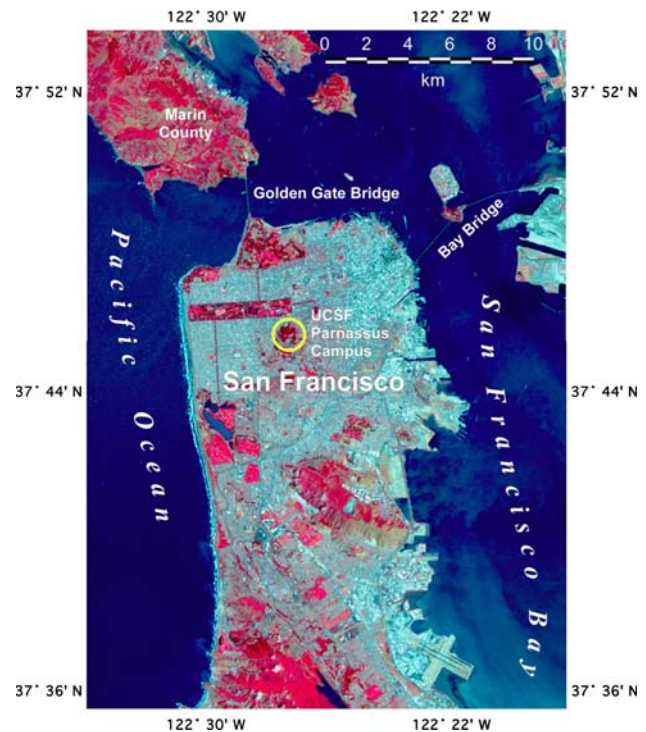

Fig. 1 Landsat false color image of the San Francisco peninsula and adjacent areas. *Red colors* denote green vegetation and *light blue colors* denote urbanized areas. The UCSF project area is marked by the *yellow circle*

project placed heavy emphasis on the collection, processing and interpretation of airborne lidar topographic data to aid in the identification of geomorphic features and conditions conducive to landsliding.

Geological setting

The general geology of San Francisco is described in many maps and reports, both published and unpublished. The Parnassus Campus lies in the San Francisco North 7.5′ quadrangle, which was mapped by Schlocker (1974) and is included in the more recent regional map compiled by Blake et al. (2000).

The geology of San Francisco is characterized by bedrock knobs and hills of Jurassic Franciscan Complex bedrock (highly deformed chert, greenstone, meta-sandstone, and shale) that protrude through such younger deposits as Quaternary alluvium, dune sand, and shallow marine sediments. The Parnassus Campus is located on a prominent Franciscan bedrock knob known as Mt Sutro. As shown in Fig. 2, the steep slopes of Mt Sutro are covered with a dense eucalyptus forest and, with the notable exception of a winding two-lane road, most of the campus infrastructure lies around its edges. Bedrock occurs at or very near the ground surface throughout much of the

Fig. 2 Color 30 cm (1 foot) raster orthophoto showing approximate extent the UCSF Parnassus Campus (*pink dashed line*) and dense forest cover on Mt Sutro. Photo source: US Geological Survey, photo date 27 February 2004

project area, but is overlain locally by surficial materials (colluvium and shallow landslides) within drainages that have developed on the steep hillsides of Mt Sutro.

Wilson et al. (2000) conducted a seismic slope stability hazard analysis of San Francisco and noted several landslides on Mt Sutro (but do not appear to have collected detailed information on the campus per se) and produced a table of susceptible geological units rather than a hazard map. Other sources of information used in this project include historical and recent borehole logs and unpublished geological and geotechnical reports on file at the consulting firm of Rutherford & Chekene, San Francisco.

Lidar data collection and processing

Lidar data for this project were collected in November 2005 by a commercial vendor as part of a project to obtain standard resolution lidar coverage of San Francisco. The vendor reduced the typical flying height from 1,400 to 900 m and collected approximately 400 ha of high-resolution lidar data covering the UCSF campus and adjacent areas with vertical accuracy conforming to the United States National Standard for Spatial Data Accuracy (NSSDA) and the Federal Emergency Management Agency (FEMA) standards, as shown for high-resolution data in Table 1. The FEMA contour interval is that which can typically be supported using the listed quality of lidar data. For normally distributed errors, approximately 68% of the measured errors should fall within the tabulated root mean squared error (RMSE) and 95% should fall within twice the tabulated RMSE. Vegetation and buildings were removed by the vendor prior to data delivery in order to produce a so-called bald earth or bare earth data set.

Compliance with the contract accuracy specifications was documented by a licensed surveyor under contract to the vendor, who collected GPS elevations at 145 points within the vendor's overall lidar project area (but outside of the more limited UCSF project area described in this paper). Measured vertical errors followed a distribution that, while not strictly normal, displayed a strong central tendency with minimal bias (Fig. 3). The RMSE of ± 0.06 m was less than the maximum acceptable value of ± 0.09 m. Horizontal errors were estimated by the vendor to be in the order of 1/3,000 of the flying altitude.

Quality assurance GPS measurements for contract compliance are generally collected in flat and open areas to reduce data analysis complications, including the contribution of horizontal errors; the practical or operational accuracy of lidar-based DEMs can be nearly an order of magnitude worse than that suggested by quality assurance measurements. In a comparison of a lidar DEM covering a portion of Seattle, Washington, with GPS measurements, Haneberg (2008) found that lidar elevation errors had a standard deviation of ± 0.75 m and statistically significant correlations with slope angle, topographic roughness, and to some extent elevation (but not slope aspect). He did not separately evaluate the effects of interpolation errors arising from different DEM gridding algorithms, which may

Table 1 Lidar vendor resolution specifications (measurements in meters)

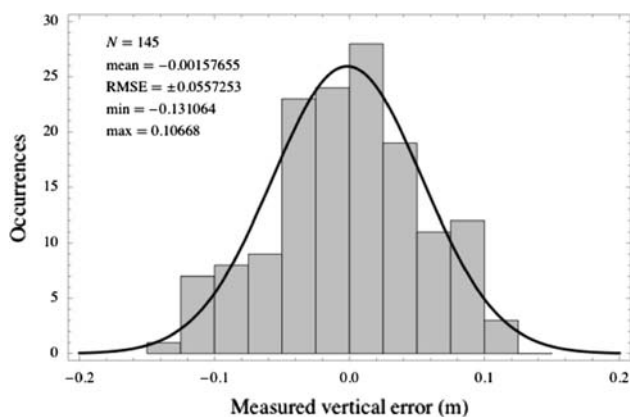| Lidar resolution	Typical flying altitude	FEMA contour interval	Typical lidar spot spacing	Allowable NSSDA RMSE
High	900	0.3	1.0	± 0.09
Standard	1,400	0.6	1.4	± 0.18
Low	2,000	1.0	1.8	± 0.30

RMSE root mean squared error

Fig. 3 Histogram of measured vertical lidar errors for 145 quality assurance points collected near, but not in, the UCSF project area by the lidar vendor. The project contract specifications called for a maximum permissible RMSE of ±0.09 m compared to the measured value of ±0.06 m. A scaled normal distribution with the measured mean and standard deviation is superimposed for comparison

also be important. The accuracy of the lidar data DEM was, however, substantially better than a conventional 10 m DEM covering the same area, which had a standard deviation of ±2.36 m (Haneberg 2006a).

The lidar data were supplied as ASCII text files containing the *xyz* coordinates and uncalibrated laser return intensity values separated into files identified as ground strikes and extracted features such as trees and buildings. Coordinates were converted by the vendor from the original WGS84 coordinates to the California State Plane Coordinate System (U.S. survey feet, NAD83 HARN horizontal datum, NAVD88 vertical datum) as preferred by both the client and principal engineering contractor.

Optimally interpolated digital elevation model

An optimally interpolated DEM was produced from the *xyz* bare earth point cloud supplied by the lidar vendor using a trial-and-error process in which two different interpolation algorithms (inverse distance squared and regularized splines with tension) and different interpolation parameters were evaluated in order to produce a DEM suitable for geological interpretation and slope hazard mapping at the UCSF site. Selection of an appropriate DEM grid spacing begins with a review of the lidar ground strike data, particularly with regard to ground strike spacing and density in geologically critical areas such as steep slopes. Care was taken to minimize obvious interpolation artifacts such as dimples or rectilinear patterns that can arise if the chosen grid is too fine, while at the same time maximizing the geological utility of the DEM. Experience has shown that the best quality DEMs useful for landform mapping are those with a grid spacing not less than 1/4 to 1/5 the typical ground strike spacing in geologically critical areas.

The DEM for this project was interpolated onto a 0.6-m (2 feet) horizontal grid using completely regularized splines with tension as implemented in the commercial raster GIS software MFWorks, with a precision of 0.01 foot (0.03 m), tension of 1.0, a block size of 1, an overlap area of 200 cells, and a sufficient sample number of 5. The advantages of creating a geologically optimal DEM rather than obtaining a DEM from the lidar vendor are addressed in the Section "Discussion" at the end of this paper.

Geomorphic derivative maps

The optimally interpolated DEM was used to create a series of geomorphic derivative maps similar to those described by Haneberg et al. (2005), Haneberg (2007), and Troost et al. (2006). These included topographic contour maps (Fig. 4), a suite of shaded relief images with different simulated illumination directions (Fig. 5), and maps depicting quantitative measures such as slope angle and topographic roughness. Although topographic roughness maps have been proven useful in other landslide studies,
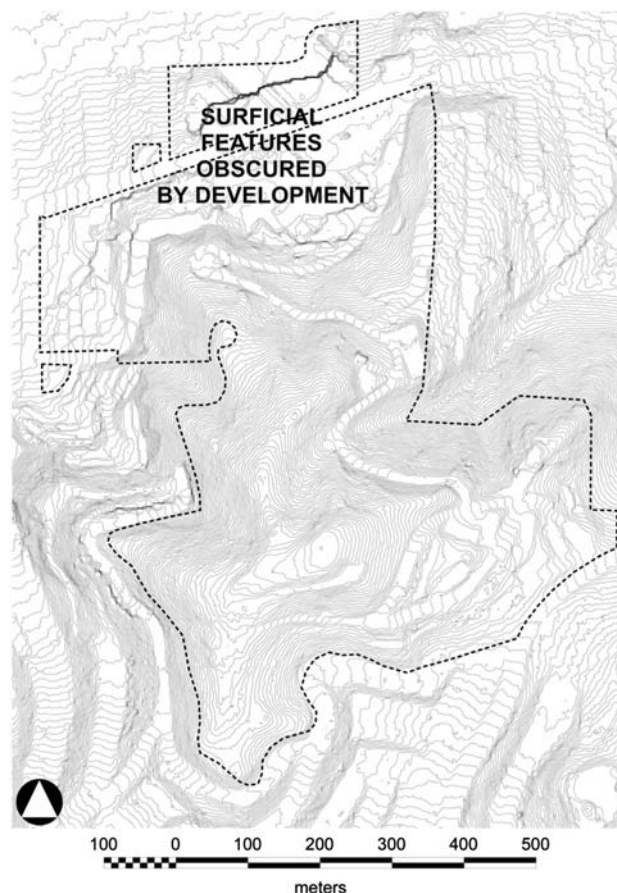

Fig. 4 Contour map of the project area based on the 0.6 m (2 foot) lidar DEM with no smoothing applied. Contour interval: 1.5 m (5 feet)

roughness maps showing eigenvalue ratios (McKean and Roering 2004) and residual deviations (Haneberg et al. 2005; Haneberg 2007) were found to be of limited utility in this study. As shown in Fig. 5a–c, shaded relief images using different simulated illumination azimuths highlight different aspects of the topography. In each part of Fig. 5a–c, the three-digit azimuth describes the direction from which the simulated illumination comes and the two-digit inclination describes the height above the horizon of the simulated light source. Figure 5d is a composite image created by adding together, in a map algebra sense, the three images in Fig. 5a–c and provides an additional view of the topography. It was found that using a suite of shaded relief images rather than a single shaded relief image can help to define subtle landforms, particularly linear features such as landslide or fault scarps.

Interpretive maps
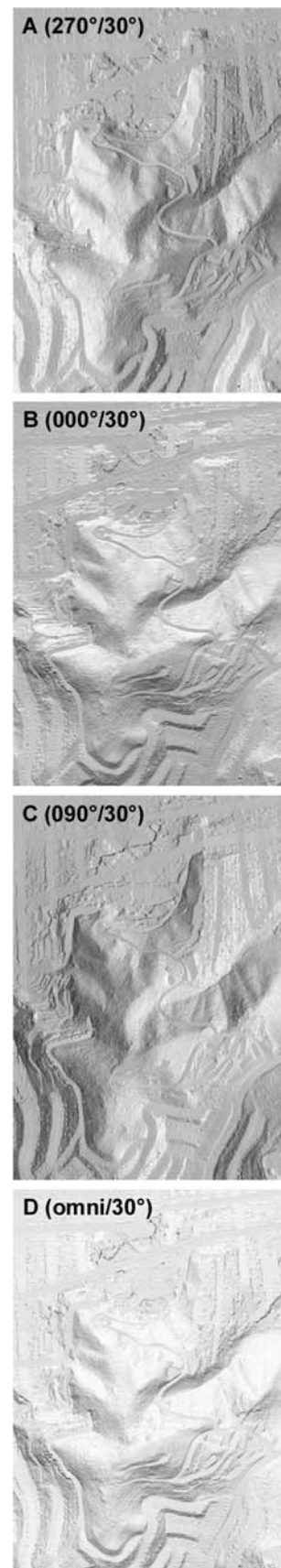
A series of three engineering geological maps were created:

(1) A standard engineering geological map using the Unified Engineering Geological Mapping System (Keaton and DeGraff 1996) to show the genesis and lithology of the mapped features,
(2) A cut and fill slope map showing areas in which natural slopes had been modified by human activity, and
(3) A slope hazard map based upon qualitative interpretations by the project team.

These are shown draped over a shaded relief image in Figs. 6, 7, and 8.

Engineering geological map

The engineering geological map (Fig. 6) was created by integrating the DEM and its derivatives with field-based observations of geological conditions. Following preliminary processing of the lidar data, fieldwork took place over 2 days in May 2006 and the map was finalized in the office to allow the use of digital mapping techniques such as the superposition of engineering geological information with the shaded relief, slope angle, roughness and contour maps.

Soil and rock types are shown on the engineering geological map using the Unified Engineering Geological Mapping System (Keaton and DeGraff 1996), with a
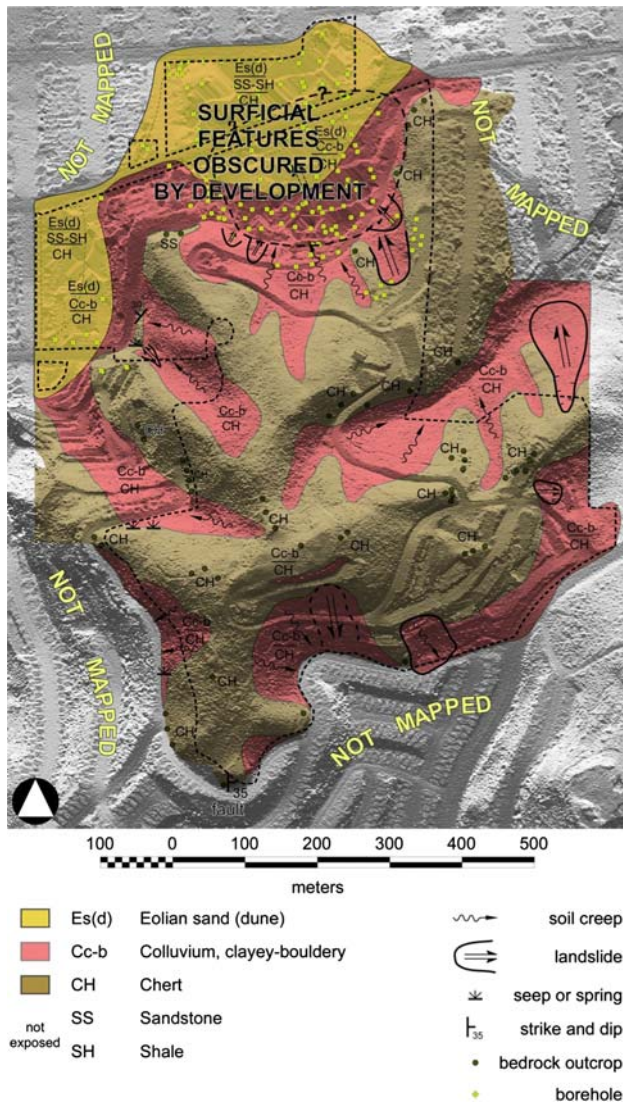
Fig. 6 Engineering geologic map draped over the omni-directional shaded relief image from Fig. 5d. Lithologic units are shown using the Unified Engineering Geologic Mapping System with stacked lithologic symbols indicating the local stratigraphy (Keaton and DeGraff 1996). *Yellow circles* indicate geotechnical borehole locations
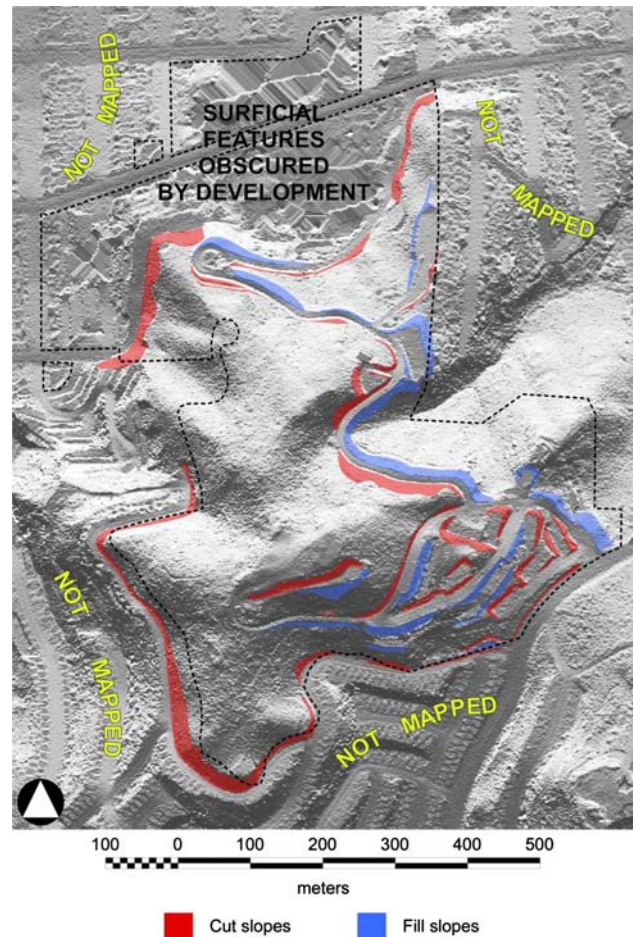

Fig. 7 Cut and fill slope map draped over the omni-directional shaded relief image from Fig. 5d. Areas of cut and fill were inferred from a combination of field observations and office based digital terrain modeling using the high-resolution lidar DEM

vertical series of soil or rock types used to indicate the stratigraphic sequence of the map units. Other features relevant to the project—for example, areas of slow soil creep, landslides and rock outcrops—are also shown on the map. Much of the area shown as chert on the engineering geological map is overlain by thin soil, but outcrops are common and the soil thickness is not likely to exceed a meter or so. Thus, the thin soil over chert was not shown on the map. Although features that may be indicative of potential future instability (for example old landslides or areas undergoing soil creep) are shown, the engineering geological map does not evaluate the likelihood of the future occurrence or severity of slope hazards.

Most of the bedrock exposed on campus is folded and thinly bedded red and green chert of the Franciscan Complex. A small area of sandstone occurs in the northwestern portion of the campus. In the few locations where strike and dip directions could be measured in the tightly folded to wavy chert beds, the orientations represent average conditions. Relatively young shallow marine sediments of the Colma Formation were encountered at depth in previous geotechnical borings but the formation is not exposed at the surface in the project area.

The engineering geological map (Fig. 6) shows a possible ancient landslide occupying much of the area beneath the most highly developed north-central portion of the campus. The ancient landslide is indicated by the large bowl-shaped feature. Identification of this feature is tentative because naturally occurring landforms indicative of landsliding have been largely destroyed by development. The large bowl-shaped feature, information from borehole logs on file at Rutherford & Chekene and an unpublished
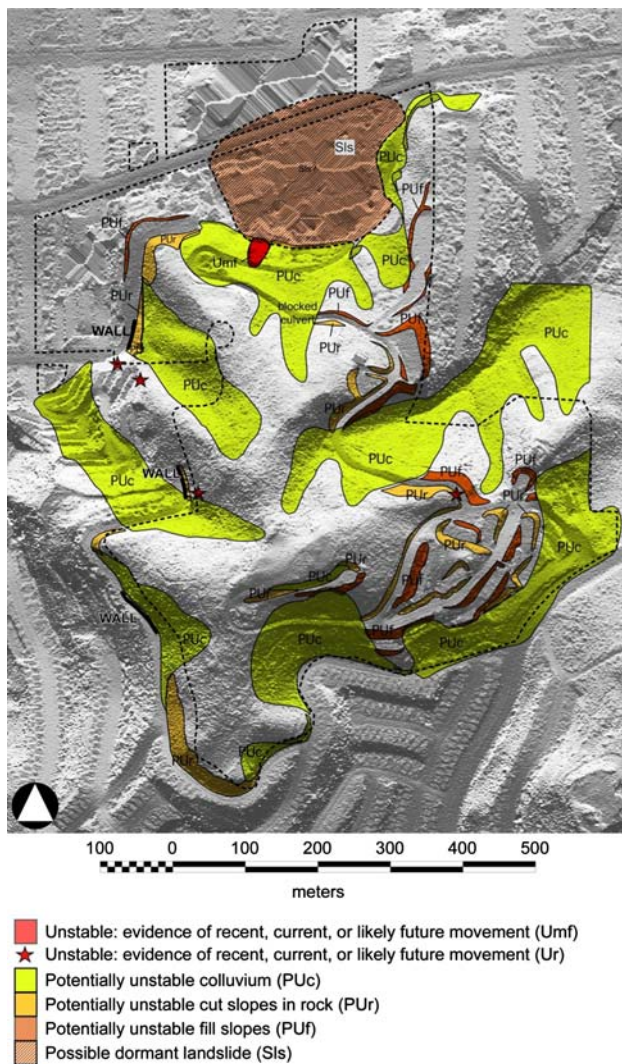
Unstable: evidence of recent, current, or likely future movement (Umf)
★ Unstable: evidence of recent, current, or likely future movement (Ur)
Potentially unstable colluvium (PUc)
Potentially unstable cut slopes in rock (PUr)
Potentially unstable fill slopes (PUf)
Possible dormant landslide (Sls)

Fig. 8 Qualitative landslide hazard map draped over the omnidirectional shaded relief image from Fig. 5d

bedrock structure contour map completed after this project were the basis of the hypothesis that the area may be underlain by a large landslide, perhaps involving Franciscan bedrock of old but uncertain age.

The possibility of a large ancient landslide in this highly developed area was raised as long ago as 1948 in a letter to the university engineer from an engineering geologist, C. Marliave (personel communication) but was discounted in later investigations by local consultants based primarily on the contention that the northward sloping sedimentary strata encountered in a campus construction project were (1) continuous and (2) bore no resemblance to the chaotic strata that had been interpreted by others to be characteristic of large ancient landslides in the region. A thorough evaluation of the potential ancient landslide, which would include a detailed subsurface synthesis supported by additional drilling and testing, was beyond the scope of this

project hence the feature is shown as a possible landslide on the engineering geological map.

Cut and fill slope map

Cut and fill slopes, which are often shown on engineering geological maps such as that in Fig. 6, were shown on a separate map for clarity (Fig. 7). Both types of slopes were identified on the basis of preliminary field observations and refined using digital terrain analysis to identify the extent of over-steepened slopes inferred to have been produced by human activity. Detailed as-built construction documents were not available, so the cut and fill slope map represents a geological interpretation based on slope form and a general knowledge of construction techniques. Some cut or fill slopes may not be shown.

Qualitative slope hazard map

The qualitative slope hazard map (Fig. 8) is an interpretive map that combines the information shown on the engineering geological map (Fig. 6), the cut and fill slope map (Fig. 7), and field observations by experienced professionals, to depict areas in which slope instability is most likely to occur. Areas with signs of very recent or imminent movement are shown in red, whereas areas with the potential for future movement as a consequence of heavy rain or seismic shaking or some combination of the two, are shown in yellow and orange. Criteria used to identify the active landslides such as that shown on Fig. 8 (map unit Umf) include bulging, cracking, seepage and general disruption of original topography. The criterion used to identify active rockfall areas (map unit Ur) was the presence of fresh boulders near the toes of slopes or adjacent roads. The yellow, light orange and dark orange units represent potentially unstable colluvium (PUc), potentially unstable cut slopes in rock (PUr) and potentially unstable fill slopes (PUf). The PUc unit corresponds to the colluvium shown on Fig. 6, which were inferred to be thicker and wetter than the thin layer of colluvium over chert in other parts of the study area. Although there is a potential for shallow landslides and debris flows in the areas shown as chert overlain by thin soil on the engineering geological map (Fig. 6), this was not included as a potential slope hazard on Fig. 8 because any such slides are likely to be small and, because of their remote locations, without much effect on campus safety or access. Areas underlain by chert and adjacent to roads, from which shallow slope failures have the potential to limit campus access, are shown as cut (PUc) or fill (PUf) slope hazards as appropriate.

The possible landslide shown on the engineering map is categorized as stable on the qualitative slope hazard map because

(1) it lies low on the slope and therefore possesses little potential energy relative to the areas it might affect,

(2) it appears to be buried and buttressed by younger sediments, and

(3) this investigation yielded no signs of recent movement, for example open cracks or deformed cultural features, in the area.

This project did not, however, include a quantitative stability evaluation of the possible landslide and the potential for future movement is unknown.

Probabilistic slope stability modeling

The high-resolution lidar DEM was used to produce physics-based probabilistic landslide hazard maps using the first-order, second-moment (FOSM) approach described by such authors as Haneberg (2000, 2004), van Westen and Terlien (1996), Wu et al. (1996), Wolff (1996), and Mankelow and Murphy (1998). The computer program PISA-m (the acronym stands for map-based Probabilistic Infinite Slope Analysis) written by Haneberg (2006b) was used to perform the calculations for this project. PISA-m takes as input a DEM, maps showing geotechnical soil units and forest cover units, and information about geotechnical parameters and their probability distributions for each map unit. Unlike previous approaches in which all of the input variables were restricted to normal distributions (van Westen and Terlien 1996; Mankelow and Murphy 1998), PISA-m accepts normal, uniform, triangular, and β-PERT distributions as well as constant values as input, calculating equivalent mean values and variances for non-normal distributions (Haneberg 2006b). PISA-m output options include maps showing the probability that the calculated factor of static safety against landsliding is less than the critical value (Prob[FS < 1]), the mean factor of safety, the standard deviation of the factor of safety, or a non-parametric slope reliability index for each raster within the DEM.

PISA-m is based on the infinite slope approximation and is therefore most useful for simulating the occurrence of landslides that are thin relative to their lengths and widths. As used in this project, the calculated probability does not explicitly include any reference to time or recurrence intervals, for example as an annual probability of landsliding. Instead, it should be interpreted as a conditional probability given the pore water pressure distributions used as input for the model. Stillwater Sciences (2007) and Weppner et al. (2008a, b) describe watershed-scale applications of PISA-m in which the pore water pressure variable was instead assigned temporal significance by using an extreme value distribution to model peak annual pore

pressure. Weppner et al. (2008a, b) further used PISA-m to simulate the change in annual probability of landsliding as a consequence of clear-cut logging by reducing the tree root strength and surcharge in areas currently covered by mature forest.

PISA-m theoretical background

Details of the FOSM approximation used in PISA-m are given in Haneberg (2000, 2004, 2006b) and briefly summarized without further reference below. The static component of the probabilistic model is based on the equation for the factor of safety against sliding, FS, for a forested infinite slope (Hammond et al. 1992):

$$FS = \frac{c_r + c_s + [q_t + \gamma_m D + (\gamma_{sat} - \gamma_w - \gamma_m)H_w D]\cos^2\beta\tan\phi}{[q_t + \gamma_m D + (\gamma_{sat} - \gamma_m)H_w D]\sin\beta\cos\beta}$$

(1)

in which c_r denotes cohesive strength contributed by tree roots (kPa), c_s cohesive strength of soil (kPa), q_t uniform surcharge due to weight of vegetation (kPa), γ_m unit weight of moist soil above phreatic surface (N/m^3), γ_{sat} unit weight of saturated soil below phreatic surface (N/m^3), γ_w unit weight of water (9,810 N/m^3), D thickness of soil above slip surface (m), H_w relative height of phreatic surface (dimensionless), β slope angle (degrees), ϕ angle of internal friction (degrees).

The influence of groundwater is incorporated using a slope-parallel phreatic surface, so that the pore water pressure is the pressure exerted by a column of water equal in height to that of the phreatic surface above a potential slip surface. This is a common but not necessary assumption for infinite slope analyses. It is, however, reasonable in cases where a relatively permeable surficial deposit is underlain by less permeable bedrock. The variable H_w represents a normalized phreatic surface height that has a range of 0–1 for non-artesian conditions.

The effects of parameter uncertainty and variability are incorporated using FOSM approximations. A mean value of FS is first calculated using the mean values of each of the independent variables, or

$$\overline{FS} = FS(\bar{x})$$

(2)

For uncorrelated independent variables, the variance (or second-moment about the mean) of FS can then be estimated by the first-order truncated Taylor series

$$s_{FS}^2 = \sum_i \left(\frac{\partial FS}{\partial x_i}\right) s_{x_i}^2$$

(3)

in which $s_{x_i}^2$ is the variance of the ith independent variable. The terms in parentheses are evaluated using mean values for each of the independent variables (implying that each of

the derivatives is a constant), and their squares are lengthy equations when all of the variables in Eq. 1 are included.

Mean values and variances for the soil properties and pore pressures were estimated on the basis of tabulated data and professional experience. The mean and variance for the slope angle at each point (r, c) within the DEM was calculated using the approximations

$$\beta_{r,c} = \arctan\left[\frac{\sqrt{(z_{r,c+1} - z_{r,c-1})^2 + (z_{r+1,c} - z_{r-1,c})^2}}{2\Delta s}\right] \tag{4}$$

and

$$s_\beta^2 = \frac{8(\Delta s)^2 s_z^2}{\left[4(\Delta s)^2 + (z_{r+1,c} - z_{r-1,c})^2 + (z_{r,c+1} - z_{r,c-1})^2\right]^2} \tag{5}$$

Based on the results of Monte Carlo simulations described in Haneberg (2004), which showed that infinite slope factors of safety followed an asymmetric lognormal-like distribution, PISA-m calculates the probability of landsliding, Prob[FS < 1], using a lognormal cumulative distribution function characterized by the calculated $\overline{FS}$ and s_{FS}^2 values.

The static method of Haneberg (2004) can be extended to include seismic slope stability by using the calculated mean factor of safety to calculate the mean Newmark (1965) yield acceleration:

$$\bar{a}_N = g(\overline{FS} - 1)\sin\bar{\beta} \tag{6}$$

in which a_N is the yield acceleration beyond which seismically induced movement can occur, FS is the static factor of safety for a slope, g is gravitational acceleration, and (for infinite slopes) β is the slope angle. The overbars indicate that in each case the mean value for each point within the DEM is used for the calculation. The calculated $\bar{a}_N$ value at each point within the DEM was then combined with the Arias intensity for a postulated earthquake to calculate the expected mean downslope movement using the regression equation developed by Jibson et al. (2000):

$$\overline{\log D_N} = 1.521\log I_A - 1.993\log\overline{a_N} - 1.546 \tag{7}$$

in which D_N is the displacement (in centimeters) of an unstable slope as a result of seismic shaking, I_A is the observed or predicted Arias intensity (m/s), and a_N is the Newmark critical acceleration with units of g. The Jibson et al. (2000) regression model has a published standard deviation of ±0.375, which is used along with the calculated mean displacement to calculate the probability that the displacement for the modeled earthquake is greater than a user specified threshold, or Prob[$D_N > D_{thresh}$]. Based on the results of numerical Monte Carlo simulations of seismic slope instability, this probability was calculated

using the assumption that D_N is log-normally distributed (Haneberg 2006a, b, 2008).

PISA-m model input

Slope angles for the probabilistic model were calculated from the DEM using a standard second-order accurate finite difference approximation as described in Eqs. 4 and 5. Soil properties were estimated using representative values for San Francisco tabulated in Wilson et al. (2000), literature compilations such as Hammond et al. (1992), and the authors' local experience. In particular, the scarcity of outcrops on the UCSF campus and small-scale structural complexity of the thinly bedded and highly deformed Franciscan chert bedrock made it impossible to make useful model-scale distinctions between favorable and adverse bedding conditions throughout the campus. Moreover, the shear strength of deformed rocks at or near the surface is controlled by discontinuities such as pervasive joints or faults. Therefore, the probabilistic model uses average values with uncertainties to reflect the structural complexity, which allows for the possibility of adverse, average, or favorable discontinuity orientations of both bedding and fractures at any given location. As discussed by Haneberg (2006a, b, 2008) DEM elevation errors are spatially correlated and can create slope angle errors that propagate into slope stability calculations. PISA-m takes elevation errors into account using Eq. 5. Based upon previous experience with lidar and conventional DEM elevation errors, we specified an elevation error standard deviation of ±3 mm (±0.01 feet) for points separated by 1.2 m (4 feet), the distance over which the slope angles are calculated by PISA-m.

Based upon our site-specific engineering geological mapping, the probabilistic analyses were conducted using two soil types (geotechnical map units): thin soil over chert and thick colluvium in valleys. As shown in Tables 2 and 3, the geotechnical variables were specified as either being random variables (in this case following either normal or

Table 2 PISA-m geotechnical parameters for soil type 1: thin soil over chert

Variable	Distribution	Mean ± SD	Minimum	Maximum
ϕ (degrees)	Normal	30 ± 1.67		
c_{soil} (kPa)	Normal	19.2 ± 6.2		
d (m)	Normal	0.76 ± 0.26		
H_w (wet)	Normal	0.50 ± 0.084		
H_w (dry)	Constant	0		
γ_{moist} (N/m³)	Uniform		15,700	18,900
$\gamma_{saturated}$ (N/m³)	Uniform		18,900	20,400
c_{roots} (kPa)	Normal	6.2 ± 1.5		
q (kPa)	Constant	0		

Table 3 PISA-m geotechnical parameters for soil type 2: thick soil in valleys

Variable	Distribution	Mean ± SD	Minimum	Maximum
ϕ (degrees)	Normal	30 ± 1.67		
c_{soil} (kPa)	Normal	19.2 ± 6.2		
d (m)	Normal	3.05 ± 0.91		
H_{w} (wet)	Normal	0.75 ± 0.084		
H_{w} (dry)	Constant	0		
γ_{moist} (N/m^3)	Uniform		15,700	18,900
$\gamma_{\text{saturated}}$ (N/m^3)	Uniform		18,900	20,400
c_{roots} (kPa)	Constant	0		
q (kPa)	Constant	0		

Fig. 9 Strong motion record used to calculate the Arias intensity of $I_A = 7.0$ m/s used as input for the seismic component of the rational probabilistic slope stability model. The record was obtained from the Pacific Earthquake Engineering Research Center (PEER) strong motion database. Record is for the Southern California Edison Lucerne station during the 1992 Landers $M = 7.3$ earthquake (direction 260°)

uniform distributions) or single-valued constants. Normally distributed variables are shown in Tables 2 and 3 using their mean values and standard deviations whereas uniformly distributed variables are shown in terms of their minimum and maximum values, although PISA-m calculates equivalent mean values and variances for the latter.

Both soil types were assigned similar shear strength parameters and unit weights, but differed in thickness, degree of saturation and tree root strength as shown in Tables 2 and 3. The assumed increased wetness of thick colluvium-filled valleys was incorporated using a dimensionless degree of saturation of $H_w = 0.75 \pm 0.084$ (mean ± SD) versus a value of $H_w = 0.50 \pm 0.084$ for the soil over chert for the static calculations to represent a range of realistically possible wet season values (no piezometric field data were available to constrain extreme pore pressure values). Tree root strength was not included in the thick colluvium unit because we inferred that root networks would not extend to the depths of potential slip surfaces and would therefore have no stabilizing effect. The seismic calculations were performed first using the same wet season values and then again with zero pore pressure to represent a dry season earthquake. Wet season pore pressure values are likely to occur during the rainy season that generally occurs between October 15 and April 15. High pore water pressure values can occur locally outside of the rainy season as the result of such artificial causes as leaking or broken water lines, storm drains, or water tanks.

The Arias intensity of the modeled earthquake was calculated from the same strong motion record used by Wilson et al. (2000) for their citywide analysis, from the Southern California Edison Lucerne station during the 1992 M7.3 Landers earthquake. Digital versions of all three components were downloaded from the Pacific Earthquake Engineering Research Center (PEER) web site and integrated to calculate Arias intensities of $I_A = 7.0$ m/s (azimuth 260°), $I_A = 6.6$ m/s (azimuth 345°), and
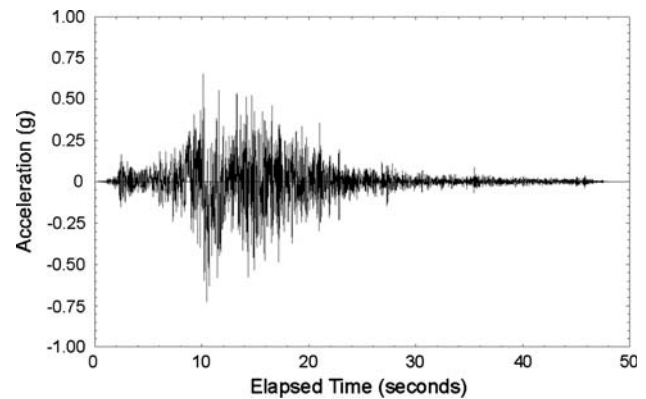
$I_A = 8.2$ m/s (vertical). The two horizontal intensities are indistinguishable from those calculated by Jibson and Jibson (2003) from the same records, and the stronger of the two horizontal intensities ($I_A = 7.0$ m/s) was chosen for the modeled earthquake. Figure 9 shows the 260° horizontal strong motion record used to calculate the $I_A = 7.0$ m/s value. A displacement threshold of 30 cm was selected for the seismic probabilistic slope stability maps, corresponding to the 30 cm threshold used to delineate high hazard areas by Wilson et al. (2000).

PISA-m model results

Results for the three probabilistic models (static wet, seismic wet, and seismic dry conditions) are shown on separate maps (Figs. 10, 11, 12). The probabilistic results share both similarities and differences with the qualitative slope hazard map (Fig. 8). Some areas shown as PUc on the qualitative slope hazard map are shown to have a low probability of landsliding on the static and dry seismic probabilistic maps. Conversely, many steep areas shown as chert covered by ostensibly stable thin soil on the qualitative slope hazard map are shown to have a high probability of landsliding on the static and dry seismic probabilistic maps. This is because the qualitative slope hazard map is based on criteria that emphasize the inferred importance of thick cohesive soil accumulations in topographic depressions such as hollows, swales and valleys. The qualitative map does not incorporate any information about steepness; thus, a relatively flat colluvium-filled valley bottom would receive the same designation as a steeper colluvium mantled slope. The qualitative model also assumes that landslides in thin soils are insignificant
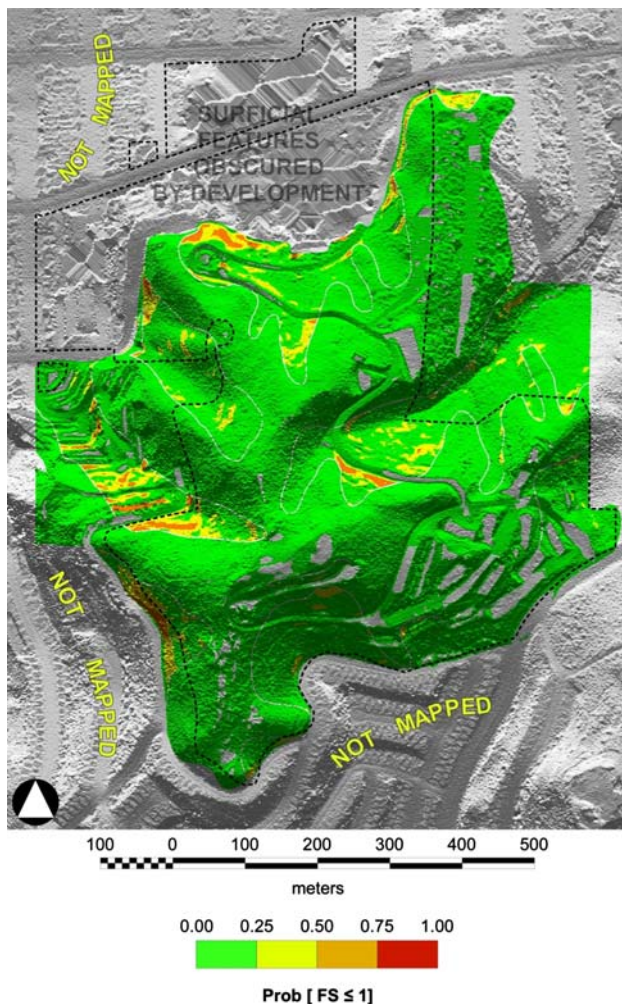
Fig. 10 PISA-m probabilistic landslide hazard map for wet static conditions, draped over the omni-directional shaded relief image from Fig. 5d. See Tables 2 and 3 for geotechnical parameters

Fig. 11 PISA-m probabilistic landslide hazard map for dry seismic conditions, draped over the omni-directional shaded relief image from Fig. 5d. See Tables 2 and 3 for geotechnical parameters

compared to landslides in thick wet colluvium in depressions, whereas the probabilistic models allow for landslides in thin soils overlying chert and explicitly take into account the fact that the thickness of cohesive soils has an effect on their stability. Figure 13 compares the total amount of potentially unstable area predicted by the three PISA-m models (Figs. 10, 11, 12) and the qualitative slope hazard map (Fig. 8). In preparing Fig. 13 it was conservatively assumed that all PISA-m modeled areas with Prob[FS < 1] ≥ 0.25 are potentially unstable. The trend is similar but the magnitudes are smaller if other thresholds, for example Prob[FS < 1] ≥ 0.50, are used.

Both the qualitative slope hazard map (Fig. 8) and the probabilistic maps (Figs. 10, 11, 12) show over-steepened cut and fill slopes to be potentially unstable even though the actual modes of failure are likely to depart from translational sliding of thin soil layers or rock slabs. Cut slope failures observed in chert and sandstone are mostly
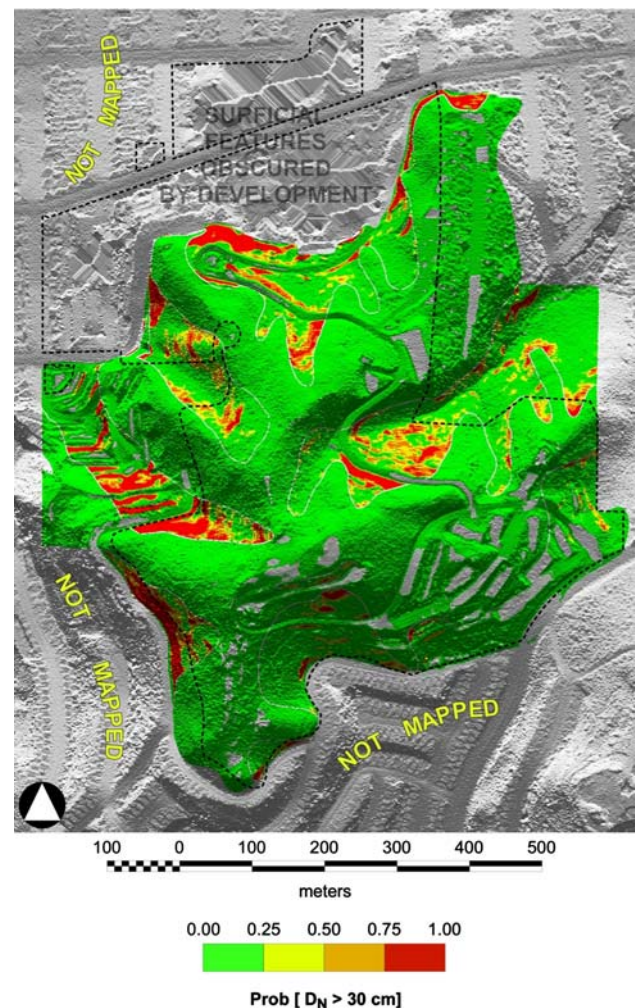
topples and wedge failures controlled by rock discontinuities. Fill slope failures are likely to be rotational.

The probabilistic models suggest that thin translational landsliding of the kind simulated by the infinite slope approximation should be restricted to a relatively small proportion of the campus under wet static conditions. Many of these potentially unstable areas, however, are adjacent to roads, buildings, and parking lots (including off-campus property). Thus, the possibility that landslides or rockfalls might block roads or partially cover parking lots during wet conditions should be taken into account by campus planners. The general spatial pattern of instability predicted for dry seismic conditions is similar to that predicted for wet static conditions, although the probability of occurrence is higher for the seismic model. Under wet seismic conditions, however, wholesale translational landsliding is to be expected in all but the flattest areas on campus. Even if the probability of a landslide occurring on flat ground is low,
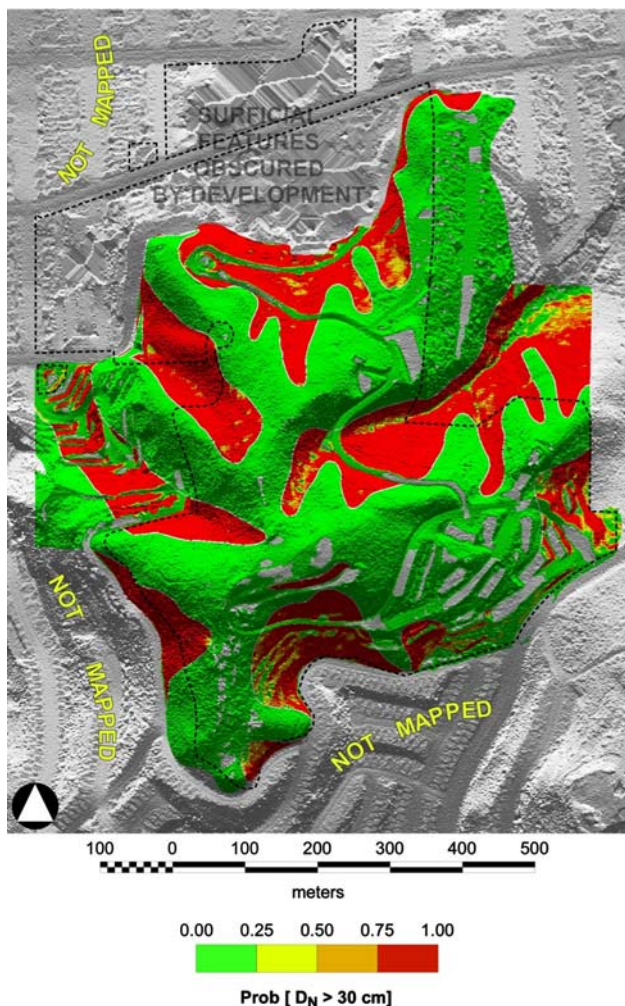
Fig. 12 PISA-m probabilistic landslide hazard map for wet seismic conditions, draped over the omni-directional shaded relief image from Fig. 5D. See Tables 2 and 3 for geotechnical parameters
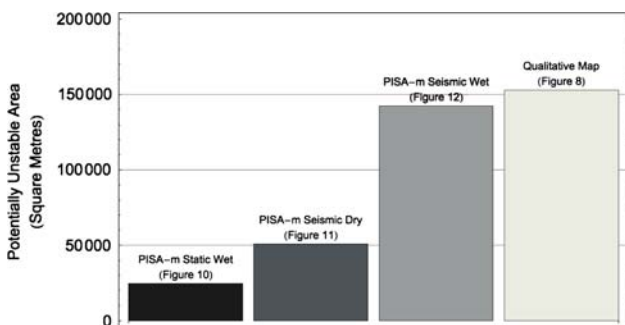

Fig. 13 Area predicted to be potentially unstable by the static wet (Fig. 10), seismic dry (Fig. 11), and seismic wet (Fig. 12) PISA-m scenarios compared to that predicted by the qualitative slope hazard map (Fig. 8)

campus plans should take into account the possibility that landslides from adjacent steep slopes may cover flat areas such as roads and parking lots.

Discussion

The combination of high-resolution lidar-based digital terrain modeling, field-based engineering geological mapping supplemented by office-based virtual mapping, and physics-based probabilistic slope stability modeling allowed an evaluation of existing and potential slope stability hazards on the steep and densely forested UCSF Parnassus Campus. Neither the mapping nor modeling could have been accomplished at the same level of detail without the lidar coverage. Traditional engineering geological mapping from aerial photographs or a photogrammetrically derived topographic base would have been too generalized for precise modeling or interpretation of slope behavior. The combination of field-based mapping, office-based virtual mapping and physics-based probabilistic modeling allowed the value of the lidar data to be maximized by going beyond a simple qualitative interpretation of shaded relief images or contour maps.

Processing of the scattered point cloud as one of the geological aspects of a project has distinct advantages over the use of DEMs created by a lidar vendor without geological considerations. Using point cloud data allows the lidar ground strike density patterns in geologically critical areas—for example, steep vegetated slopes—to be critically examined by experienced geologists, geomorphologists, or geotechnical engineers. Ground strike spacing can influence the detail shown on a gridded DEM and control the scales of features that can be identified in different parts of a project area. Regardless of the supposed resolution of a DEM, geomorphic features smaller than the actual ground strike spacing in different parts of a project area will not be depicted. The authors' experience has been that landforms with characteristic dimensions less than an order of magnitude greater than the ground strike spacing, which can range from decimeters to meters or tens of meters in different parts of the study area, cannot be reliably recognized. Ground strikes in forested areas also tend to be clustered in space. Thus, the ability to superimpose a lidar ground strike map during virtual mapping sessions in the office can help to show the minimum size of features that one might hope to resolve and map in different parts of the project area. Working with the point cloud data also allows experienced geo-professionals to experiment with different gridding algorithms and parameters with the objective of producing a DEM that is optimized for landform mapping in a particular project area.

The benefit of creating a set of derivative maps is that, whereas only a finite number of paper maps can be carried in the field, an almost infinite number of map combinations can be created electronically for preliminary office interpretation before fieldwork and virtual map refinement after fieldwork. For example, the geologist can create

combinations such as a shaded relief image with illumination from the east draped with a color map of slope angles and 1.5 m contour lines and then alternate shaded relief maps to see if his or her interpretations change. Supporting imagery such as aerial orthophotos, multispectral images, or historical geological maps can also be included if available, particularly if the work is done within a GIS framework that supports the use of files with different projections, coordinate systems and geodetic datums. For this project, contour maps with a 1.5-m contour interval proved to be the most useful base for engineering geological mapping in the field.

The study indicated that physics-based probabilistic modeling using PISA-m can be a useful tool for evaluating extreme or rare conditions such as very wet slopes or large earthquakes. Field-based engineering geological mapping can provide critical information about recent or current slope instability. Precise forecasting of the areal consequences of rare, extreme, or unprecedented events based on field observations, however, is difficult if not impossible. Thus, observation and modeling are best used as complementary—rather than mutually exclusive—approaches in order to leverage the value of lidar digital elevation data.

Comparison of the qualitative slope hazard map (Fig. 8) with the three PISA-m maps (Figs. 10, 11, 12) shows that the qualitative map produced using field observations and geologic inference corresponds to a worst-case scenario, namely a strong earthquake during a wet period, with a very low likelihood of occurrence in any given year (Fig. 13). The PISA-m probability threshold required to produce a worst-case result similar to the qualitative slope hazard map, moreover, is a conservative value of Prob[FS < 1] ≥ 0.25. Thus, the qualitative slope hazard map is not only a worst-case assessment, it is a conservative worst-case assessment. This is because geologic inference is likely to integrate a wide range of possible future conditions that include extreme events and, even with detailed lidar-based topographic maps, qualitative field observations cannot effectively incorporate highly localized changes in slope angle. As such, maps such as Fig. 8 are likely to greatly overestimate the landslide hazard associated with all but the most extreme triggering events. Because it uses a highly detailed DEM and information about soil properties in physics-based calculations, however, PISA-m is able to delineate highly localized areas susceptible to sliding under specific conditions. For example, note that the only active landslide shown along the campus road on Figs. 6 and 8, which occurred under wet static conditions before the lidar data were collected, is adjacent to an area of elevated probability on the wet static PISA-m map (Fig. 10). Only the toe of the active landslide has a high PISA-m wet static probability of sliding because the head of the landslide decreased in slope when the

movement occurred. It is reasonable to assume that the entire area of the active landslide would have fallen into a higher wet static probability class had the topography not been modified by landsliding.

The results presented in this paper beg the question, when should the qualitative maps based on geologic inference be used and when should quantitative physics-based probabilistic maps such as those produced by PISA-m be used? A traditional qualitative map such as Fig. 8 might be used when one requires a conservative and all-inclusive worst-case assessment that takes into account a wide range of triggers (rainfall, earthquakes, construction) over an indeterminate time period. The PISA-m maps might be used when one requires a detailed assessment or comparison of the hazard posed by specific triggers (for example, the degree to which the static landslide hazard is compounded by the rare occurrence of a major earthquake compared to a moderate earthquake), perhaps over a specified time period if time-dependent pore pressure probabilities are used (as in Weppner et al. 2008a, b). Ideally, the decision should be made with the participation of the parties who will be assuming the attendant risks (e.g., project owners, residents, insurers, and/or regulators) and are in a position to make informed decisions about acceptable degrees of hazard and risk. There may be cases, for example in the design or location of critical facilities such as hospitals, fire stations, or power plants in which conservative worst-case assessments are justified. In other cases—for example, the construction of lightly used roads in remote areas—such assessments may be overly conservative and unjustified.

References

Ardizzone F, Cardinali M, Galli M, Guzzetti F, Hovius N, Peruccacci S, Reichenbach P, Rossi M, Stark CP (2006) Identification and mapping of landslides using lidar technology. Geophys Res Abstr 8:05603 SRef-ID: 1607-7962/gra/EGU06-A-05603

Blake MC, Graymer RW, Jones DL (2000) Geologic map and map database of parts of Marin, San Francisco, Alameda, Contra Costa, and Sonoma Counties, California. Miscellaneous Field Studies Map MF-2337. U.S. Geological Survey, Reston

Delano HL, Braun DD (2007) PAMAP lidar-based elevation data: a new tool for geologic and hazard mapping in Pennsylvania. Geol Soc Am Abstr Programs 39(6):167

Drazba MC, Inglish AR, Burns S (2006) Mapping landslide thresholds, using lidar in the West Hills of Portland, Oregon. Geol Soc Am Abstr Programs 38(7):563

Falls JN, Wills CJ, Hardin BC (2004) Utility of lidar survey for landslide mapping of the Highway 299 corridor, Humboldt County, California. Geol Soc Am Abstr Programs 36(5):331

Glenn NF, Streutker DR, Chadwick DJ, Thackray GD, Dorsch SJ (2005) Analysis of lidar-derived topographic information characterizing and differentiating landslide morphology and activity. Geomorphology 73(1–2):131–148. doi:10.1016/j.geomorph.2005.07.006

Hammond C, Hall D, Miller S, Swetik P (1992) Level I stability analysis (LISA) documentation for version 2.0. General Technical Report INT-285. Forest Service, Intermountain Research Station, U.S. Department of Agriculture, Ogden, 190 p

Haneberg WC (2000) Deterministic and probabilistic approaches to geologic hazard assessment. Environ Eng Geosci 6:209–226

Haneberg WC (2004) A rational probabilistic method for spatially distributed landslide hazard assessment. Environ Eng Geosci 10(1):27–43. doi:10.2113/10.1.27

Haneberg WC (2006a) Effects of digital elevation model errors on spatially distributed seismic slope stability calculations: an example from Seattle, Washington. Environ Eng Geosci 12(3):247–260. doi:10.2113/gseegeosci.12.3.247

Haneberg WC (2006b) PISA-m: map-based probabilistic infinite slope analysis, version 1.0. User manual. Haneberg Geoscience, Seattle. http://www.haneberg.com/manual_1_0_1.pdf. Accessed 8 July 2008

Haneberg WC (2007) Large-scale terrain visualization using SRTM digital elevation models: an example from the Indian Himalaya. Geol Soc Am Abstr Programs (39)6:166

Haneberg WC (2008) Elevation errors in a LIDAR digital elevation model of West Seattle and their effects on slope stability calculations. In: Baum RL, Godt J, Highland L (eds) Landslides and engineering geology of the Greater Seattle area, Washington. Geological Society of America Reviews in Engineering Geology, vol 20. Geological Society of America, Boulder, pp 55–66

Haneberg WC, Creighton AL, Medley EW, Jonas DA (2005) Use of lidar to assess slope hazards at the Lihir gold mine, Papua New Guinea. In: Hungr O, Fell R, Couture R, Eberhardt E (eds) Landslide risk management: proceedings of international conference on landslide risk management, Vancouver, Canada, 31 May to 3 June, 2005, Supplementary CD. A. A. Balkema, New York

Jibson RW, Jibson MW (2003) Java programs for using Newmark's method and simplified decoupled analysis to model slope performance during earthquakes (version 1.1). U.S. Geological Survey Open-File Report 03-005 (CD-ROM). U.S. Geological Survey, Reston

Jibson RW, Harp EL, Michael JA (2000) A method for producing digital probabilistic seismic landslide hazard maps. Eng Geol 58:271–289

Keaton JR, DeGraff JV (1996) Surface observation and geologic mapping. In: Turner AK, Schuster RL (eds) Landslides, investigation and mitigation. Transportation Research Board Special Report 247. Transportation Research Board, Washington, DC, pp 178–230

Mankelow JM, Murphy W (1998) Using GIS in the probabilistic assessment of earthquake triggered landslide hazards. J Earthquake Eng 2(4):593–623

McKean J, Roering J (2004) Objective landslide detection and surface morphology mapping using high-resolution airborne laser altimetry. Geomorphology 57:331–351

Newmark NM (1965) Effects of earthquakes on dams and embankments. Geotechnique 15:139–160

Roering JJ, Kirchner JW, Dietrich WE (2005) Characterizing structural and lithologic controls on deep-seated landsliding: implications for topographic relief and landscape evolution in the Oregon Coast Range, USA. Geol Soc Am Bull 117(5/6):654–668. doi:10.1130/B25567.1

Sato HP, Yagi H, Moarai M, Iwahashi J, Sekiguchi T (2007) Airborne lidar data measurement and landform classification mapping in Tomari-no-tai landslide area, Shirakami Mountains, Japan. In: Sassa K, Fukuoka H, Wang F, Wang G (eds) Progress in Landslide Science. Springer, Berlin, pp 237–249

Schlocker J (1974) Geology of the San Francisco North Quadrangle, California. U.S. Geological Survey Professional Paper 782. U.S. Geological Survey, Washington DC, 109 p

Schulz WH (2006) Landslide susceptibility revealed by lidar imagery and historical records, Seattle, Washington. Eng Geol 89(1–2):67–87. doi:10.1016/j.enggeo.2006.09.019

Stillwater Sciences (2007) Landslide hazard in the Elk River basin, Humboldt County, California. Unpublished consulting report. Stillwater Sciences, Arcata

Troost KG, Wisher AP, Haneberg WC (2006) A multifaceted approach to high-resolution geologic mapping of Mercer Island, near Seattle, Washington. Geol Soc Am Abstr Programs 37(7):164

Van Den Eeckhaut M, Poesen J, Verstraeten G, Vanacker V, Nyssen J, Moeyersons J, van Beek LPH, Vandekerckhove L (2006) Use of lidar-derived images for mapping old landslides under forest. Earth Surf Processes Landforms 32(5):754–769. doi:10.1002/esp.1417

van Westen CJ, Terlien MTJ (1996) An approach towards eterministic landslide hazard analysis in GIS: a case study from Manizales (Columbia). Earth Surf Processes Landforms 21(9):853–868. doi:10.1002/(SICI)1096-9837(199609)21:9<853::AID-ESP676>3.0.CO;2-C

Weppner E, Hoyt J, Haneberg WC (2008a) Slope stability modeling and landslide hazard in Freshwater Creek and Ryan Slough, Humboldt County, California: unpublished consulting report. Pacific Watershed Associates, Arcata, 72 p

Weppner E, Hoyt J, Haneberg WC (2008b) Lidar-based landslide hazard modeling using PISA-m, SHALSTAB, and SMORPH, Freshwater Creek and Ryan Slough watershed, Humboldt County, California. Eos Trans AGU 89(53) (Fall Meeting Supplement, Abstract H41K-04)

Wilson RI, Wiegers MO, McCrink TP (2000) Earthquake-induced landslide evaluation report. In: Seismic Hazard Zone Report for the City and County of San Francisco, California. California Division of Mines and Geology Seismic Hazard Zone Report 043. California Division of Mines and Geology, San Francisco, pp 19–39

Wolff TF (1996) Probabilistic slope stability in theory and practice. In: Shackleford CD, Roth MJS (eds) Uncertainty in the geologic environment: from theory to practice. Proceeding, Uncertainty '96, American Society of Civil Engineers Special Paper 58. American Society of Civil Engineers, New York, pp 419–433

Wooten RM, Latham RS, Witt AC, Douglas TJ, Gillon KA, Fuemmeler SJ, Bauer JB, Nickerson JG, Reid JC (2007) Landslide hazard mapping in North Carolina—geology in the interest of public safety and informed decision making. Geol Soc Am Abstr Programs 39(2):76

Wu TH, Tang WH, Einsten HH (1996) Landslide hazard and risk assessment. In: Turner AK, Schuster RL (eds) Landslides, investigation and mitigation. Transportation Research Board Special Report 247. Transportation Research Board, Washington, DC, pp 106–118